**ARTICLE**

Check for updates

# Reversible $Zn^{2+}$ Insertion in Tungsten Ion-Activated Titanium Dioxide Nanocrystals for Electrochromic Windows

Yi Liang[1], Sheng Cao[1] ✉, Qilin Wei[1], Ruosheng Zeng[1], Jialong Zhao[1], Haizeng Li[2] ✉, William W. Yu[3], Bingsuo Zou[1] ✉

## HIGHLIGHTS

- A reversible $Zn^{2+}$ insertion in anatase $TiO_2$ nanocrystals is reported for the first time.

- This is the first report regarding $TiO_2$ for zinc-anode-based electrochromic devices, which will subsequently broaden its applications to zinc-ion electrochemical cells.

- A prototype device based on the $TiO_2$ nanocrystals delivers a high optical modulation, fast response times, and robust electrochemical stability.

**ABSTRACT** Zinc-anode-based electrochromic devices (ZECDs) are emerging as the next-generation energy-efficient transparent electronics. We report anatase W-doped $TiO_2$ nanocrystals (NCs) as a $Zn^{2+}$ active electrochromic material. It demonstrates that the W doping in $TiO_2$ highly reduces the $Zn^{2+}$ intercalation energy, thus triggering the electrochromism. The prototype ZECDs based on W-doped $TiO_2$ NCs deliver a high optical modulation (66% at 550 nm), fast spectral response times (9/2.7 s at 550 nm for coloration/bleaching), and good electrochemical stability (8.2% optical modulation loss after 1000 cycles).

**KEYWORDS** Electrochromism; Smart windows; $TiO_2$; Doping; $Zn^{2+}$-based electrochromic
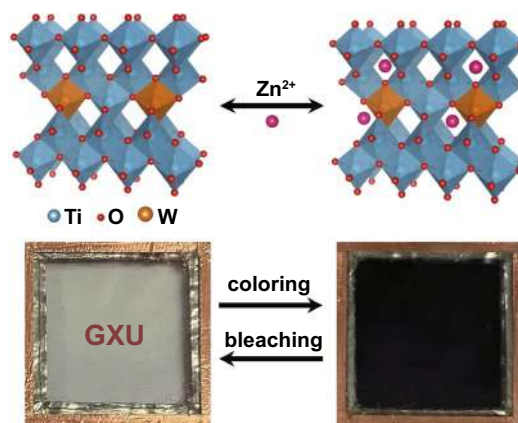
✉ Sheng Cao, caosheng@gxu.edu.cn; Haizeng Li, haizeng@sdu.edu.cn; Bingsuo Zou, zoubs@gxu.edu.cn

1 MOE Key Laboratory of New Processing Technology for Non-Ferrous Metals and Materials, and Guangxi Key Laboratory of Processing for Non-Ferrous Metals and Featured Materials, School of Physical Science and Technology, Guangxi University, Nanning 530004, People's Republic of China

2 Institute of Frontier and Interdisciplinary Science, Shandong University, Qingdao 266237, People's Republic of China

3 Department of Chemistry and Physics, Louisiana State University, Shreveport, LA 71115, USA

# 1 Introduction

Electrochromic smart windows can alter the solar radiation transmittance by a small applied voltage according to the weather conditions and/or personal preferences, which reduces the energy consumption of lighting and cooling/heating of a room [1–9]. The basic working principle of electrochromism is that the color or optical properties of certain electroactive materials change reversibly by redox reactions through intercalation/delamination of electrolyte ions [1, 5, 10, 11]. Monovalent $H^+$ and $Li^+$ are the most used electrolyte ions in current electrochromic devices [12, 13]. Due to the limited reserves and high reactivity of Li metal and the strong corrosion tendency of acidic $H^+$, the use of these electrolytes will inevitably increase the preparation cost and/or shorten the operation lifetime, thus limiting the real-world applications of electrochromic devices [5, 14–16]. Multivalent cations (e.g., $Al^{3+}$, $Mg^{2+}$, $Zn^{2+}$) are more promising for electrochromism because they provide multiple charges compared to the monovalent $Li^+$ and $H^+$ [17–23]. This, as a result, will lead to a decrease in the amount of inserted cations and is expected to enhance the electrochromic performance, including rapid switching times and good cycling stability [24, 25]. In addition, some of the multivalent ions are compatible with aqueous electrolytes, which shows great advantages in operational safety and low production cost [17, 20, 24, 26]. Therefore, multivalent metal ions are gradually considered as superior alternatives to construct high-performance electrochromic devices.

Among various multivalent metal ions, $Zn^{2+}$ is regarded as superior to others to trigger the electrochromism due to its simplified preparation process and nontoxicity [15, 20, 25, 27]. Furthermore, the relatively low redox potential of $Zn^{2+}/Zn$ (−0.763 V versus standard hydrogen electrode), which shows good compatibility with pH-neutral aqueous electrolytes and thus inhibiting the occurrence of hydrogen evolution reaction [28–32]. As a result, the pH value of the electrolyte will be stable during the device cycling. This, therefore, will significantly enhance the cycling stability of the devices [30, 33]. All these merits enable the ZECDs to become the state-of-the-art focus in the electrochromic community [15, 16, 20, 26, 27, 29, 34]. However, due to the high polarization and narrow voltage window characteristics of $Zn^{2+}$ electrochemical reactions [29, 35], it is challenging to find a suitable electrochromic material as the host for the intercalation of $Zn^{2+}$. To date, the existing ZECDs, almost all utilizing the classical electrochromic material (*i.e.*, $WO_3$) as the cathode [16, 20, 27, 34], suffer from the corrosion of $WO_3$ in aqueous acidic electrolyte. Therefore, it is of significant urgency to explore other cathodic electrochromic materials that can provide the same coloration ability while possessing a better electrochemical stability than $WO_3$ for a better implementation of the smart windows in practice.

Titanium dioxide ($TiO_2$) is a cathode material with excellent physical, chemical stability, and acid resistance, which has been proved to have excellent electrochromic properties in $Li^+$-based electrolytes [4, 12, 13, 36–39]. However, there is still no report regarding $TiO_2$ for Zn-ion electrochemical cells from both the electrochromic and battery community yet. This is mainly attributed to the fact that divalent $Zn^{2+}$ possesses a larger size and stronger coulombic ion lattice interactions than monovalent cations of $Li^+$. As theoretically predicted from the thermodynamic mechanism, reducing the intercalation energy of ions can activate the reversible electrochemical behavior of known materials [40]. For example, the intercalation energy of $Mg^{2+}$ and $Al^{3+}$ is significantly reduced by introducing Ti vacancy into anatase $TiO_2$, and thus reversible multivalent ion batteries with high efficiency and high capacity can be built [18]. Further exploration based on this work to activate $Zn^{2+}$-triggered electrochemical (*e.g.*, electrochromic, energy storage properties) behavior of $TiO_2$ should generate new superior performances in the electrochromic and battery applications.

In this work, we report the $Zn^{2+}$-triggered electrochromic properties of $TiO_2$ nanocrystals (NCs) for the first time. To implement the above-mentioned conjecture, colloidal W-doped $TiO_2$ NCs were firstly prepared by a fluoride-assisted controlled synthesis method. The as-synthesized doped $TiO_2$ NCs showed a single anatase phase with a uniform size distribution. The electrochromic characterization in three-electrode measurements shows that the W-doped $TiO_2$ NCs exhibit reversible electrochromic properties that are driven by $Zn^{2+}$. The optical modulation range reaches as high as 77.6%, and the coloration and bleaching times are 10.4 and 2.2 s, respectively. Density functional theory (DFT) calculations confirm that that W doping $TiO_2$ reduces the ion intercalation energy of $Zn^{2+}$, thus activating the reversible $Zn^{2+}$-triggered electrochromic properties of $TiO_2$. The real-world applications of W-doped $TiO_2$ NCs are also demonstrated in prototype electrochromic devices. The demonstrated devices confirm the good $Zn^{2+}$ electrochromic performance with high optical modulation (66% at 550 nm), fast spectral response times (9/2.7 s at 550 nm for coloration/ bleaching), and good electrochemical stability (the transmittance loss at 550 nm is 8.2% after 1000 cycles).

## 2 Experimental Section

### 2.1 Synthesis of Colloidal W-Doped TiO$_2$ NCs

All preparations were performed in a Schlenk line system under flowing nitrogen (N$_2$). Briefly, 1 mmol titanium ethoxide (technical grade), 0.1 mmol tungsten chloride, 8 mL 1-octadecene (90%,), 10 mmol 1-octadecanol (99%), 0.5 mL oleic acid (90%), 0.5 mL oleylamine (90%), and 0.4 mmol ammonium fluoride (NH$_4$F, > 98%) were mixed in a 50 mL three-neck flask. After 20 min of vacuum degassing at 120 °C, the mixture was heated quickly to 280 °C in N$_2$ atmosphere and kept at this temperature for 1 h for NC growth. After being cooled to ~ 60 °C, the solid NC samples were obtained by precipitation with acetone as well as a centrifugal procedure with 7000 rpm for 2 min. After that, the supernatant solution was discarded and the precipitation was re-dispersed in hexane for repeated centrifugal cycles (i.e., three times of the centrifugal procedure). Finally, the NCs were re-dispersed in toluene with a concentration of ~ 45 mg mL$^{-1}$ for use. W-doped TiO$_2$ with nominal W contents from 0 to 20 atom % was produced by varying the amount of tungsten chloride in the starting mixture while keeping all other synthesis parameters fixed.

### 2.2 Fabrication of W-Doped TiO$_2$ NC Film

A 2 × 2 cm$^2$ FTO glass (10 Ω sq$^{-1}$) was thoroughly cleaned with 2 vol% Hellmanex III solution for 5 min, rinsed with deionized water, and then washed with acetone and ethanol for 15 min each. 100 μL of the TiO$_2$ NC solution (~ 45 mg mL$^{-1}$) was then spin-coated onto the FTO glass at 1500 rpm for 30 s. After drying on a hot plate at 250 °C for 5 min, a second spin-coating was applied. The spin-coating processes were repeated for five times to build up the desired film thickness. The as-deposited doped TiO$_2$ NC film on FTO glass was then heated in air at 400 °C for 50 min (5 °C min$^{-1}$) to remove the organic ligands.

### 2.3 Assembly of an Electrochromic Device

The demonstrated device was assembled with zinc foil as an anode sandwiched between two W-doped TiO$_2$ (W4) NC film cathode electrodes. The three electrodes were assembled into an optical unit facing each other and separated by 3 M double-sided adhesive tape. A syringe was used to inject 1 M ZnSO$_4$ electrolyte into the device. The assembled device was then sealed by transparent glue.

### 2.4 Characterization

The composition, morphology, and structure of NCs were characterized by field emission scanning electron microscopy (FESEM, ZEISS SIGMA 500/VP) with energy-dispersive X-ray spectroscopy (EDS, using an INCA x-act attachment, Oxford), transmission electron microscope (TEM, FEI TECNAI G2 F30), X-ray powder diffraction (XRD, Rigaku corporation), Raman microscope (Raman, WITec, with a 532 nm Nd:YAG laser exciting source), and X-ray photoelectron spectroscopy (XPS, ESCALAB 250 XI +). The XPS peaks were curve-fitted by the XPSPeak41 software. Binding energies were corrected by referencing the C 1 s peak of adventitious carbon to 284.8 eV. In situ transmittance spectra of the films and devices were performed on an AVANTES spectrometer (AvaSpec-ULS2048CL-EVO). Electrochemical tests were carried out using an AUTOLAB PGSTAT204 electrochemical workstation.

### 2.5 Electrochemical and Electrochromic Measurements

The electrochemical and electrochromic properties of doped TiO$_2$ NC films were measured by using a custom-made three-electrode spectroelectrochemical cell connected to an AVANTES spectrometer. For the standard Zn$^{2+}$ intercalation and de-intercalation measurements, a three-electrode in which Zn foil was used as counter electrode and reference electrode, and 1 M ZnSO$_4$ was used as working electrolyte. The transmittance of an FTO glass that had undergone the same heat treatment as the working electrode in the same electrolyte was used as the baseline. All potentials were quoted with respect to a Zn$^{2+}$/Zn standard. Switching time ($\tau$) was defined as the time to achieve 90% of the full modulation in the specified potential range. Coloration efficiency (CE) was calculated by the formula: $CE = \Delta OD/\Delta Q = \log(T_b/T_c)/\Delta Q$, where $\Delta Q$ was the injected charge. All transmission spectra for different applied voltages were measured by the AVANTES spectrometer.

### 2.6 Computation Details

The diffusion barriers of $Zn^{2+}$ were calculated by climbing image nudged elastic band (NEB) method with a force-based optimization scheme. The structure optimization was implemented in the Vienna ab initio simulation package (VASP) based on DFT. To study single $Zn^{2+}$ migration in anatase $TiO_2$ and W-doped $TiO_2$, supercell structures of $1 \times 2 \times 1$ and $2 \times 2 \times 1$ were constructed by using the unit cell of anatase $TiO_2$. The atomic number of pure $TiO_2$ is $Ti_{16}O_{32}$. In pure $TiO_2$ with supercell structures of $1 \times 2 \times 1$ and $2 \times 2 \times 1$, one of Ti is replaced by W to construct W-doped $TiO_2$ structure with the atomic number of $Ti_7WO_{16}$ and $Ti_{15}WO_{32}$. A Zn atom is adsorbed on the surface of $Ti_{16}O_{32}$ and diffused from one structural site to another. The same calculation method is used in $Ti_7WO_{16}$ and $Ti_{15}WO_{32}$. In detail, we give the calculated energy barrier of $Zn^{2+}$ diffusion on the (001) surface, which takes the initial structure (0) as the zero point, the x-axis is the length of Zn atom in the Zn atom distance (0) structure, and the y-axis is the energy of each structure minus the energy of (0) structure, that is, if it is positive, the energy of this position is higher than (0), and if it is negative, it is lower than (0).

## 3 Results and Discussion

### 3.1 Preparation, Morphology, and Microstructure of W-doped $TiO_2$ NCs

A series of W-doped $TiO_2$ colloidal NCs with different W contents were prepared through a modified fluoride-assisted one-pot method [37] by varying the W to Ti atomic ratio in the precursor mixture. Note that the oxygen anion in the $TiO_2$ lattice prepared by this method is not replaced by the F anion (Fig. S1). The W to Ti precursor ratios of 0%, 5%, 10%, and 20% were denoted as W0, W1, W2, and W4. The energy-dispersive X-ray spectroscopy (EDS) results revealed that the actual W doping level of W0, W1, W2, and W4 were 0%, 1.09%, 2.38%, and 4.11%, respectively (Table S1). The content of W by EDS (a bulk analysis) is slightly lower than that by X-ray photoelectron spectroscopy (XPS, a surface analysis, Table S1), indicating that more W atoms are distributed on the surface of NC. The morphology of the as-synthesized W-doped $TiO_2$ NCs is shown in Fig. 1a–d. It is found that all the samples were pseudospherical, with

diameter distributions of $8.6 \pm 2.0$, $7.1 \pm 1.5$, $7.0 \pm 2.0$, and $5.5 \pm 1.3$ nm for W0, W1, W2, and W4, respectively. It is apparent that an increase in the dopant content decreased the NC size, which may be attributed to the effect of the W ions on crystal growth rate through surface charge modification [41].

Figure 1e compares the XRD patterns of W-doped $TiO_2$ NCs with reference data (JCPDS No. 21–1272) of bulk $TiO_2$ [37, 42]. All samples exhibit the anatase $TiO_2$ structure with no signs of an impurity phase. It is found that the line width of diffraction peaks for all doped $TiO_2$ NCs becomes wider with an increase in W concentration, suggesting that the size of NCs decreases with W doping and that is consistent with the TEM observation. The (101) diffraction peak in the right panel shift to lower $2\theta$ values with an increase in W, which indicates that the unit cell expands with the incorporation of W ions into the $TiO_2$ lattice [43]. This shift is also evidence of lattice doping where W ions with a larger effective ionic radius replacing smaller Ti ions [42]. The microstructure of W-doped $TiO_2$ was further characterized by Raman spectroscopy. As shown in Fig. 1f, the typical anatase peaks at 159 $cm^{-1}$ ($E_g$), 522.6 $cm^{-1}$ ($A_{1g}$), and 646.2 $cm^{-1}$ ($E_g$) are observed in all samples [38, 44]. The absence of other Raman peaks in all doped samples further indicates that there is no other heterophase. The expanded view of the low-frequency $E_g$ peak is shifted from 159.3 to 169.3 $cm^{-1}$ with the increasing W doping level. Since the $E_g$ peak is a characteristic Ti−O stretching mode, when Ti ions in the lattice are replaced by W ions, this shift can be used as another favorable evidence for W entering the lattice of $TiO_2$ [44]. It has been reported that the ion radius of $Ti^{4+}$ is 0.60 Å, while the ionic radii of the dopant ions are $W^{6+}$(0.60 Å)/$W^{5+}$(0.62 Å). The small difference between the dopant and host ionic radii is the reason why W replaces the Ti ions in the oxide lattice [42, 43]. These measurements confirm that the W ions have been successfully incorporated into the $TiO_2$ lattice, and the produced W-doped $TiO_2$ NCs present a single anatase phase.

### 3.2 $Zn^{2+}$-based Electrochemical and Electrochromic Performance of W-Doped $TiO_2$ NCs

To evaluate the effect of W doping on the $Zn^{2+}$ electrochromic properties of $TiO_2$ NCs, these NCs were spin-coated on FTO glass and then heat-treated in the air up to 400 °C to
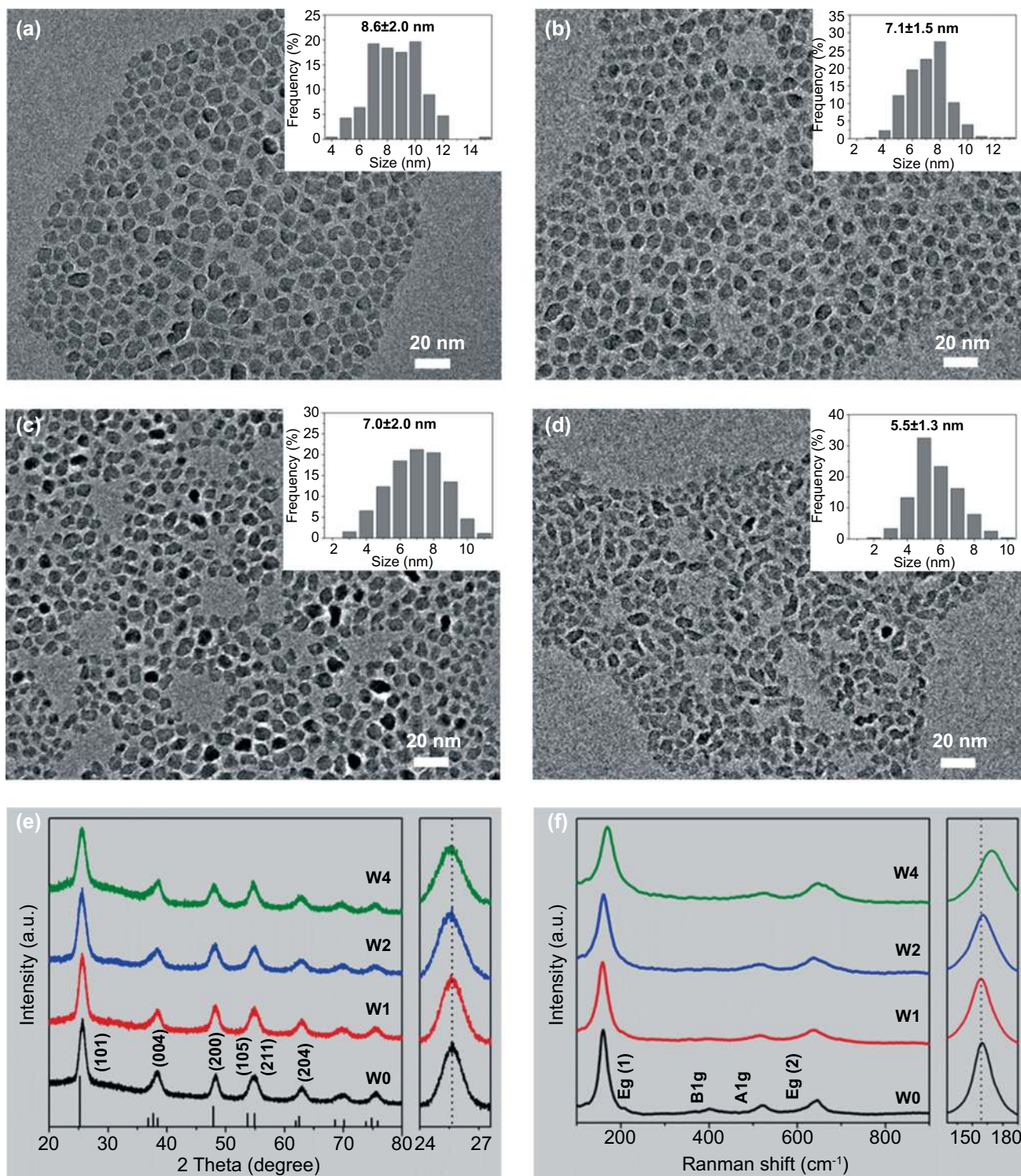
**Fig. 1** Morphologies and Structural evolution of W-doped $TiO_2$ NCs with different W doping content. **a–d** are TEM images and size distributions (inserts) for W0, W1, W2, and W4, respectively. **e** XRD patterns. The right panel shows the magnified (101) diffraction peaks. **f** Raman spectra. The right panel shows the shift of $E_g$ (1) peaks

remove surfactant and form transparent conductive NC film. Scanning electron microscopy (SEM, Fig. 2a) indicates that the W-doped $TiO_2$ NC film is uniform and the thickness of the film is 480 nm. The $Zn^{2+}$ electrochemical and electrochromic properties of doped $TiO_2$ NC films were characterized by a three-electrode spectroelectrochemical cell, which is configured with 1 M $ZnSO_4$ electrolyte and Zn sheets as counter electrode and reference electrode. To intuitively evaluate the effect of W doping on $Zn^{2+}$ electrochromic, W0 and W4 were selected for comparative study in the main text, while the information of other samples was included in the Supporting Information (Figs. S2–S4). Figure 2b shows the cyclic voltammograms (CVs) of W0 and W4 films at a scanning rate of 1 mV $s^{-1}$ in a potential range of 0–1.3 V

(vs. $Zn^{2+}$/Zn). It can be seen that the current density of W4 film is much higher than that of W0 film, indicating that W doping improves the $Zn^{2+}$ electrochemical performance of $TiO_2$ NCs (Fig. S2). Compared with $TiO_2$ NCs, the $Zn^{2+}$ diffusion coefficient in W-doped $TiO_2$ NCs is significantly improved (Fig. S3), which further indicates that W doping in $TiO_2$ NCs can activate the kinetics of $Zn^{2+}$ electrochemistry. Figure 2c exhibits the transmittance spectra of W0 and W4 films under fully bleached (1.3 V for 30 s) and fully colored states (0 V for 30 s). The wavy transmittance spectra and the > 100% transmittance of the bleached electrochromic film are attributed to the constructive interference [3, 5]. For undoped $TiO_2$ NC film, it is found that the optical transmittances between colored and bleached states change very little
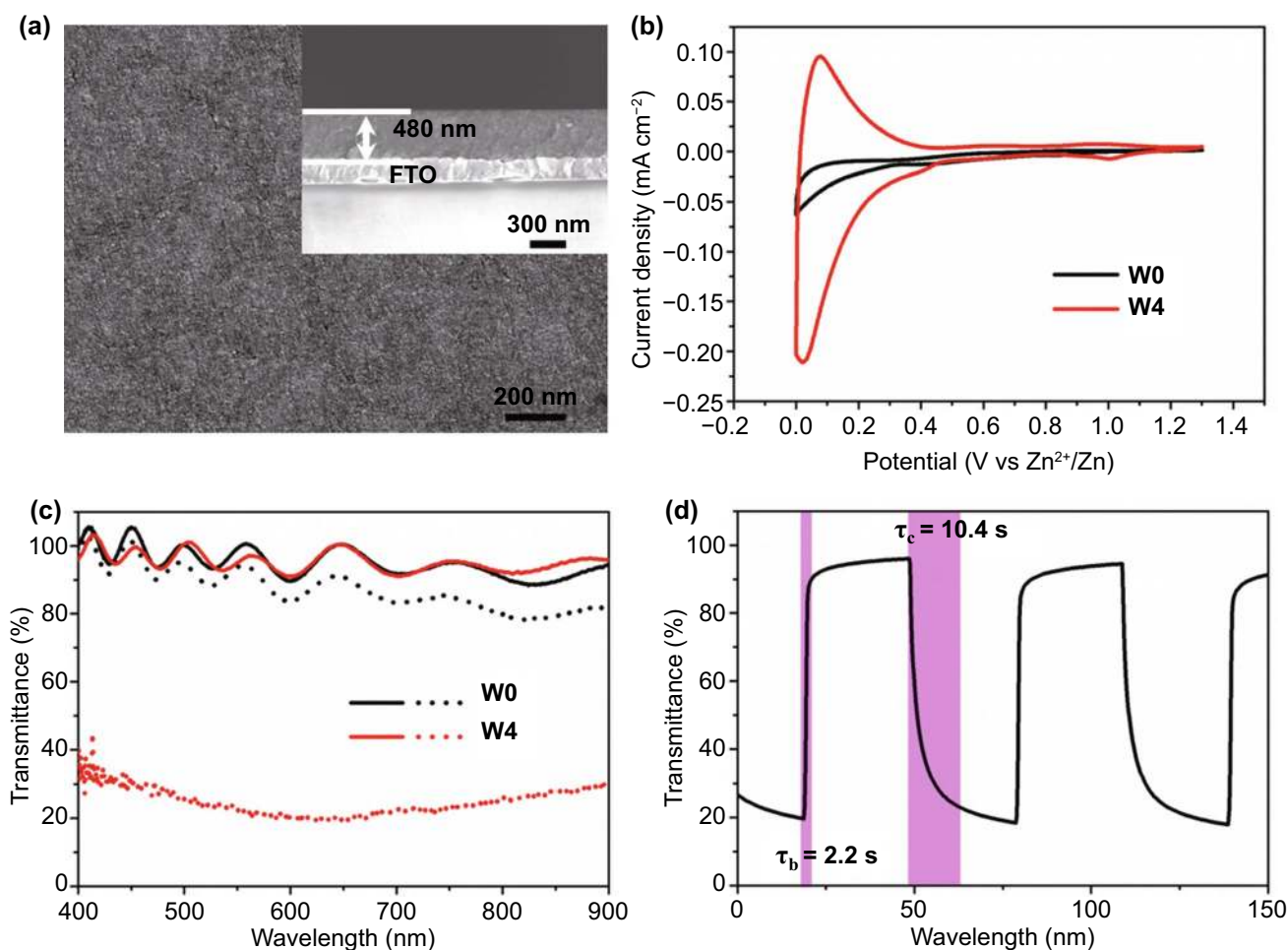


**Fig. 2** Characterizations of W-doped $TiO_2$ NC films. **a** Surface and cross-sectional (inset) SEM images of a W4 film. **b** Voltammograms of the $TiO_2$ and W4 NC films at 1 mV $s^{-1}$ in the 0–1.3 V (vs. $Zn^{2+}$/Zn) window in 1 M $ZnSO_4$ aqueous electrolyte. **c** Optical transmittance spectra of the $TiO_2$ and W4 NC films at fully colored (dot lines) and bleached (solid lines) states. **d** In situ optical transmittance of a W4 NC film at 550 nm in potential steps of 0–1.3 V

(*i.e.,* 5% at 550 nm). The poor electrochromic properties of pure anatase $TiO_2$ NCs may be due to the strong Coulomb lattice interaction [24], which leads to the ineffective intercalation of $Zn^{2+}$ ions into $TiO_2$ lattice. While for the W-doped $TiO_2$ NC film, although the transmittance of the bleached state is almost the same as that of undoped $TiO_2$ NC film, the transmittance of the colored state is much lower than that of W0 film (Figs. S4 and S5). Since the different sizes of the W0 and W4 NCs, the electrochromic properties of pure $TiO_2$ NCs with similar size to W4 were characterized to reveal the effect of NC size on the electrochromic properties. The two sizes of pure $TiO_2$ NCs have the almost same spectral modulation range (Fig. S6), indicating that the size of NCs has a limited effect on the $Zn^{2+}$ electrochromic properties. The above results therefore clearly indicate that W doping remarkably boosts the $Zn^{2+}$ electrochromic properties of $TiO_2$ NCs.

Figure 2d shows the dynamics in the electrochromic modulation of the optical response of the W-doped $TiO_2$ NC film electrode. It is observed that the transmittance modulation of W-doped $TiO_2$ film at 550 nm reaches 77.6%, and the coloration time ($\tau_c$) and bleaching time ($\tau_b$) are 10.4 and 2.2 s, respectively. The coloration efficiency of this film is 37.3 $cm^2\ c^{-1}$ (Fig. S7), which is equivalent to the typical electrochromic properties of $TiO_2$ [4, 8, 37]. The high transmittance modulation (77%) and response time ($\tau_b/\tau_c = 7.9/5.8$ s)

monitored at 633 nm were also observed (Fig. S8); all these properties can be compared with the best available $Zn^{2+}$ electrochromic materials (Table S2) as well as the typical electrochromic properties of $TiO_2$ (Table S3) reported. Since $Li^+$-based electrolytes are still the most used electrolyte in an electrochromic device. Therefore, the comparison electrochromic properties of W-doped $TiO_2$ NC films in $Li^+$- and $Zn^{2+}$-based electrolytes (the concentration of $Li^+$ is 2 times higher than that of $Zn^{2+}$) were performed (Fig. S9). The optical contrast in $Li_2SO_4$ electrolyte is 408% lower than that in $ZnSO_4$ electrolyte, and the coloring efficiency of W4 obtained in $Li_2SO_4$ electrolyte is lower than that in $ZnSO_4$ electrolyte, indicating that W-doped $TiO_2$ NCs have better electrochromic properties driven by $Zn^{2+}$ ions. These measurements demonstrate that the as-synthesized W-doped $TiO_2$ NCs can be an alternative $Zn^{2+}$ electrochromic material to meet the needs of next-generation smart windows.

### 3.3 Mechanism Analysis of $Zn^{2+}$-based Electrochromic of W-doped $TiO_2$ NCs

The ex situ XPS and in situ Raman spectra of W-doped $TiO_2$ NC films were conducted to investigate the $Zn^{2+}$ electrochromic mechanism. As shown in Fig. 3a, there is no Zn XPS signal in the initial electrode, but there is an obvious Zn 2p peak in the fully colored state, indicating
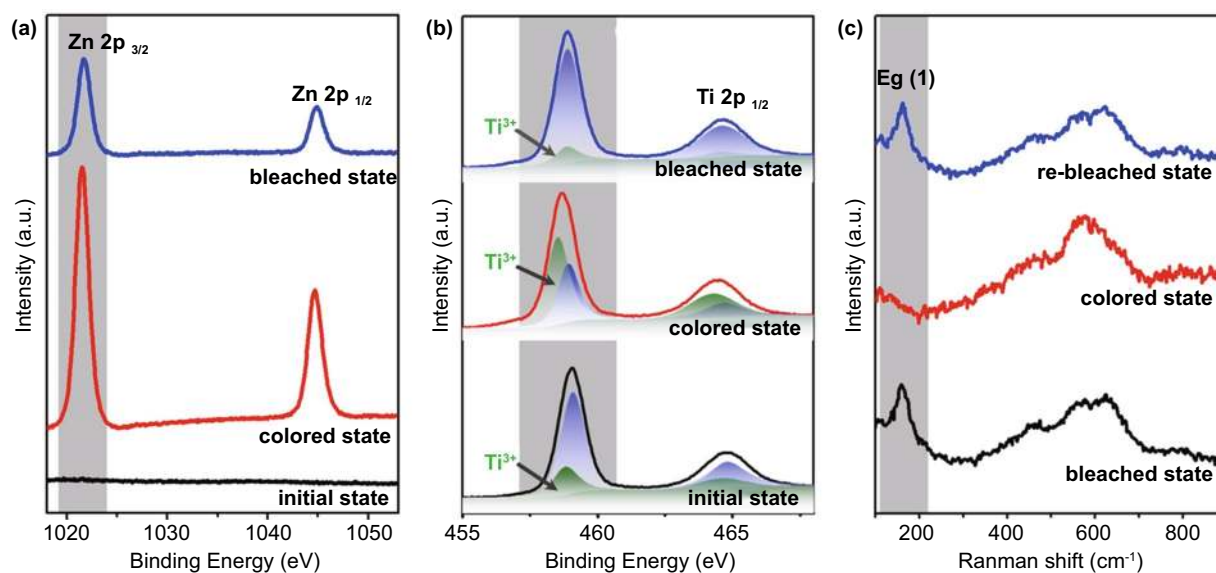


**Fig. 3** Structural evolution of a W-doped $TiO_2$ NC film during the $Zn^{2+}$ electrochromic process. **a–b** Ex situ high-resolution XPS spectrum of Zn 2p (**a**) and Ti 2p (**b**) in the initial, colored (0 V) and bleached (1.3 V) states. **c** In situ Raman spectra during the colored and bleached states

that $Zn^{2+}$ ions are successfully intercalated into the host of $TiO_2$. The peak of Zn 2p still appears in the bleached state, which indicates that a portion of the intercalated $Zn^{2+}$ ions is trapped in the "deep" sites with high-energy barriers during the electrochromic cycles. The trapped $Zn^{2+}$ ions can be extracted from the "deep" $Zn^{2+}$ sites by applying a high current under a stable voltage window of the electrolyte for real applications [12, 45]. The peak area of Zn 2p of the bleached state is far smaller than that of the coloration state, which confirms the (de-)insertion of $Zn^{2+}$. Figure 3b shows that the Ti $2p_{3/2}$ peak at the initial state can be divided into two peaks, corresponding to $Ti^{3+}$ $2p_{3/2}$ and $Ti^{4+}$ $2p_{3/2}$, respectively, at 458.5 and 458.9 eV [8, 46]. The calculated area ratio of $Ti^{3+}$ to $Ti^{4+}$ is 1/3, which is consistent with the fact that the $TiO_2$ matrix remains electrically neutral after Ti is replaced by high valence W. After being fully colored at 0 V, the peak of Ti 2p shifts to higher binding energy. The obvious change of binding energy can be attributed to the change of coordination environment of titanium with zinc and oxygen atoms. Due to the reduction in $Ti^{4+}$ to $Ti^{3+}$ in the process of $Zn^{2+}$ ion insertion, the two peaks become wider, and the ratio of $Ti^{3+}$ 2p increases. The area ratio of $Ti^{3+}$ to $Ti^{4+}$ is calculated to be 2/1. Therefore, the high optical transmittance contrast of the W-doped $TiO_2$ NC films may be due to the reduction in $Ti^{4+}$ to $Ti^{3+}$ during the $Zn^{2+}$ ions intercalation [47]. At the fully bleached state at 1.3 V, the Ti 2p spectra almost return to the initial state after the extraction of $Zn^{2+}$. The coordination environment and valence state of W also changed during the electrochromic process (Fig. S10). However, the reduction ratio of $W^{6+}$ is much lower than that of $T^{4+}$, which indicates that W mainly contributes to the activation of the $Zn^{2+}$-based electrochromic performance of the doped $TiO_2$ system. Figure 3c shows the Raman spectra of the W4 electrode in different states. There are obvious anatase $TiO_2$ $E_g$ peak in the initial state and bleached state, but it disappears in the colored state, which indicates the coordination environment of Ti–O was changed in the $Zn^{2+}$ intercalation process [44]. No new diffraction peak appears in the NC film at bleached and colored state (Fig. S11), suggesting that the anatase $TiO_2$ phase is maintained throughout the electrochromic process. The above results show that in W-doped $TiO_2$ NCs, due to the intercalation of $Zn^{2+}$, the injected electrons are localized in $Ti^{4+}$, resulting in the blue shift of absorption band, which leads to the obvious color change.

To reveal the influence of W doping on the $Zn^{2+}$ electrochromic properties of activated $TiO_2$, the diffusion barriers of $Zn^{2+}$ in anatase $TiO_2$ and W-doped $TiO_2$ were further studied by DFT calculation [40, 48]. Figure 4 shows the diffusion energy curves of isolated $Zn^{2+}$ from one stable position to a neighboring one in the $TiO_2$ and W-doped $TiO_2$. It can be seen that in anatase $TiO_2$, the barrier energy required for the diffusion of a $Zn^{2+}$ adsorbed on the surface from one structural site to another is 2.56 eV; while for W-doped $TiO_2$ with a W content of 4.2%, the barrier energy required for the diffusion of adjacent structural sites is only 0.86 eV. The decrease in the $Zn^{2+}$ diffusion barrier in W-doped $TiO_2$ was also found at the doping level of 2.1% (Fig. S12), which may be due to the distortion of the $TiO_6$ octahedron caused by the introduction of W dopant ions [18, 30, 49]. In general, this small diffusion barrier is more conducive to the diffusion of $Zn^{2+}$ ions in the lattice, thus activating the $Zn^{2+}$ electrochemical reaction of $TiO_2$. The DFT calculation results are in good agreement with the above experimental results, indicating that W doping in anatase $TiO_2$ is a facile way to improve the electrochemical kinetics of $Zn^{2+}$ ions in the matrix and activate the $Zn^{2+}$ electrochromic properties.
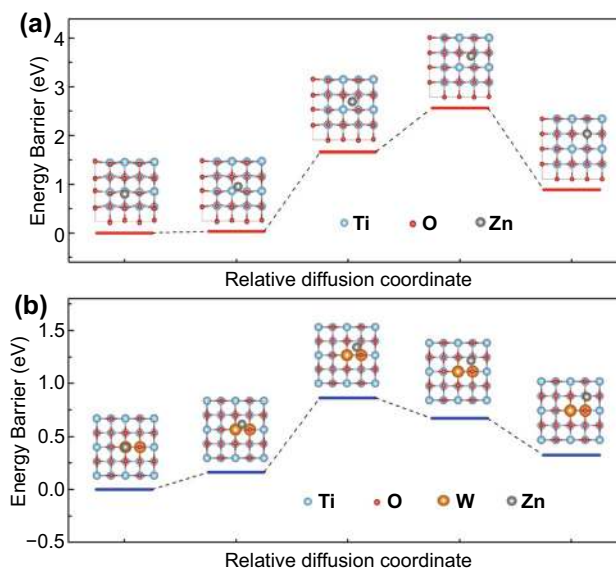


**Fig. 4** DFT calculations. The diffusion energy curves of isolated $Zn^{2+}$ from one stable position to a neighboring one in the **a** $TiO_2$ and **b** doped $TiO_2$ with a W content of 4.2%. Insets show the possible $Zn^{2+}$ insertion sites in $TiO_2$ and W-doped $TiO_2$ during the diffusion process
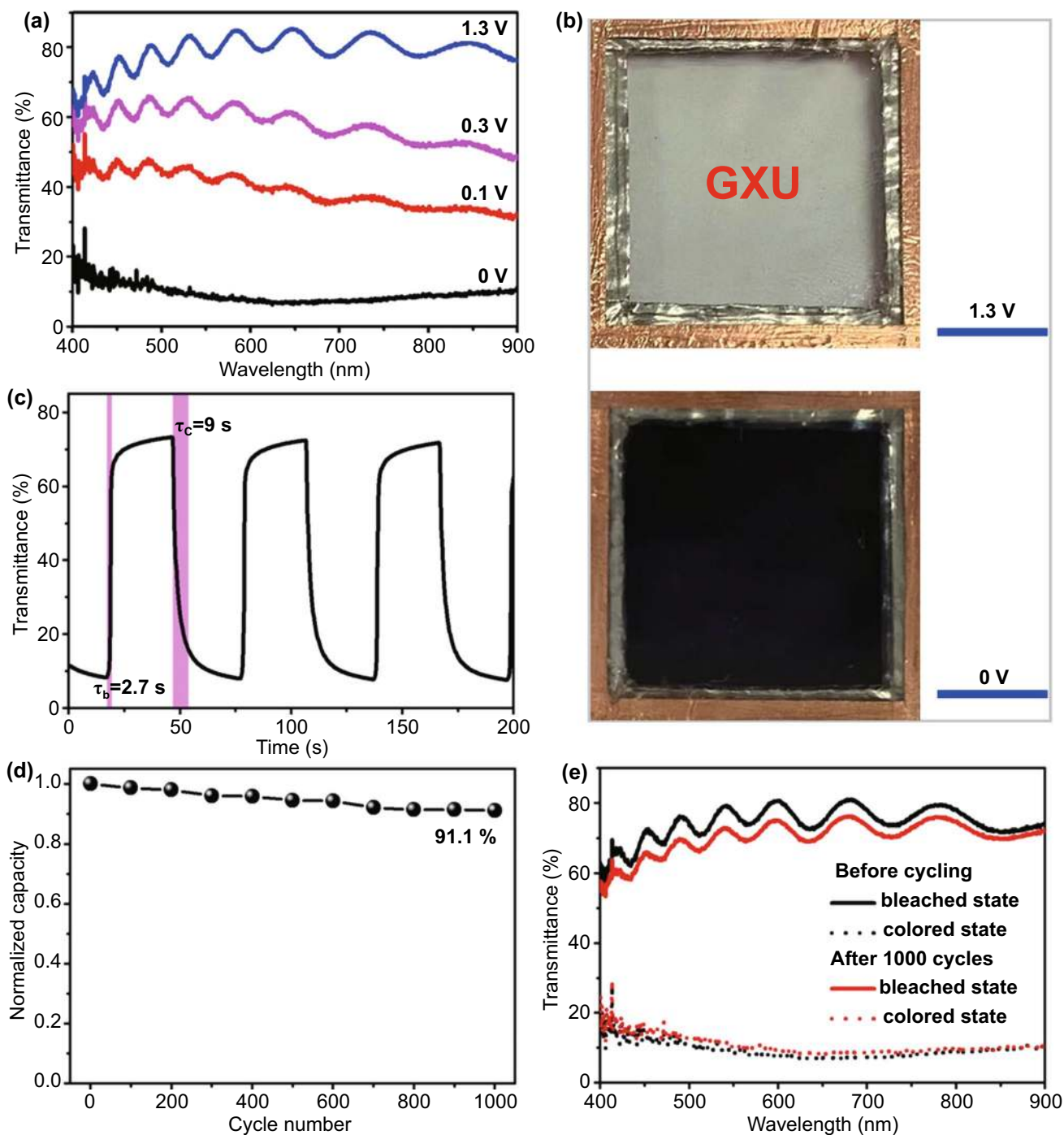
Fig. 5 Electrochromic performance of demonstration device prepared by W4 sample. **a** Transmittance spectra at different operating voltages. **b** Photographs at fully bleached and colored state. The blue scare bar is 1 cm. **c** Real-time transmittance spectra of the device at 550 nm at 1.3–0 V. **d** Normalized charge capacity profile over 1000 voltammetric cycles at 20 mV s$^{-1}$ between 0 and 1.3 V. **e** Optical transmittance spectra before and after 1000 cycles at fully bleached and colored states

## 3.4 Zn$^{2+}$-based Electrochromic Performance of Demonstration Device

For the demonstration of actual use of high performance of Zn$^{2+}$ electrochromic, a prototype device is assembled by sandwiching zinc foil anode between two electrochromic W4 NC film electrodes and filled with 1 M ZnSO$_4$ electrolyte [16]. Figure 5a shows that the demonstrative device delivers similar good Zn$^{2+}$ electrochromic performance as in the three-electrode measurements, and the optical modulation range is as high as 66% at 550 nm. The optical modulation range of the device is slightly lower than that of the W4 single electrode measured in a three-electrode electrochemical cell due to the extra transmission loss of the second electrode in the sandwich structure. Figure 5b shows the corresponding photos of the device under fully bleached and colored states, showing a high coloration contrast of the bright and dark images. The optical response was characterized by in situ spectroscopy at 550 nm (Fig. 5c). The result discloses that the device shows fast spectral response and the coloration time $\tau_c$ and bleaching time $\tau_b$ are 9 and 2.7 s, respectively. The device also shows good bistability (Fig. S13). After the device being colored at 0 V for 30 s, the optical transmission is only increased by 5.7% and 5.1% at 550 and 633 nm after 3600 s, respectively. The cycle stability of the device was evaluated by CV at the commonly used scan rate of 20 mV s$^{-1}$ [3, 50]. It is found that the cycle stability of the W-doped TiO$_2$ NC thin film was good (Fig. S14), retaining 91.1% of its first-cycle (integrated) charge capacity after 1000 electrochemical cycles (Fig. 5d). Meanwhile, the high coloration contrast (Fig. S15) and the fast response time (Table S4) are also kept well in the electrochemical cycling, and the coloration contrast at 550 nm is 60.4% after 1000 cycles (Fig. 5e). This indicates that the decrease in transmittance modulation at 550 nm after 1000 cycles was just 8.2%. It is discovered that the surface morphology and structure of W4 film are almost unchanged after cycling, which shows a dense film structure comprised of anatase NCs (Figs. S16 and S17). This further indicates that TiO$_2$ has excellent crystal structure stability and is suitable for the fabrication of ZECDs. These electrochromic performances indicate that the prototype device fabricated by W-doped TiO$_2$ NCs is comparable to the state-of-the-art ZECDs (Table S5).

## 4 Conclusions

In summary, we reported an effective method of W doping to boost Zn$^{2+}$ electrochromic performance of anatase TiO$_2$ NCs. The colloidal W-doped TiO$_2$ NCs were prepared by a fluoride-assisted synthesis. The as-synthesized W-doped TiO$_2$ NCs were a single anatase phase with uniform size distribution. The electrochromic characterization in a three-electrode measurement showed that they exhibited reversible electrochromic properties driven by Zn$^{2+}$. The optical modulation range at 550 nm reached 77.6%, and the coloration and bleaching times were 10.4 and 2.2 s, respectively. DFT calculations illustrated that W doping in TiO$_2$ reduced the ion intercalation energy of Zn$^{2+}$, thus activating the reversible Zn$^{2+}$ insertion electrochromic properties of TiO$_2$. The prototype ZECDs with W-doped TiO$_2$ NCs were fabricated, which showed high optical modulation of 66% at 550 nm, fast spectral response time (9/2.7 s for coloration/bleaching), and good electrochemical stability (the optical modulation at 550 nm was only 8.2% after 1000 cycles). This work demonstrates that the W-doped TiO$_2$ NCs are a promising Zn$^{2+}$-active electrochromic material and also suggests that TiO$_2$ can be a promising material for other electrochemical applications such as zinc ion batteries.

## References

1. S.M. Islam, T.S. Hernandez, M.D. McGehee, C.J. Barile, Hybrid dynamic windows using reversible metal electrodeposition and ion insertion. Nat. Energy **4**, 223–229 (2019). https://doi.org/10.1038/s41560-019-0332-3

2. G. Cai, J. Wang, P.S. Lee, Next-generation multifunctional electrochromic devices. Acc. Chem. Res. **49**, 1469–1476 (2016). https://doi.org/10.1021/acs.accounts.6b00183

3. S. Zhang, S. Cao, T. Zhang, Q. Yao, A. Fisher et al., Monoclinic oxygen-deficient tungsten oxide nanowires for dynamic and independent control of near-infrared and visible light transmittance. Mater. Horiz. **5**, 291–297 (2018). https://doi.org/10.1039/c7mh01128h

4. S. Cao, S. Zhang, T. Zhang, Q. Yao, J.Y. Lee, A visible light-near-infrared dual-band smart window with internal energy storage. Joule **3**, 1152–1162 (2019). https://doi.org/10.1016/j.joule.2018.12.010

5. Z. Wang, X. Wang, S. Cong, F. Geng, Z. Zhao, Fusing Electrochromic technology with other advanced technologies: a new roadmap for future development. Mater. Sci. Eng. R Rep. **140**, 100524 (2020). https://doi.org/10.1016/j.mser.2019.100524

6. Y. Yao, Q. Zhao, W. Wei, Z. Chen, Y. Zhu et al., $WO_3$ quantum-dots electrochromism. Nano Energy **68**, 104350 (2020). https://doi.org/10.1016/j.nanoen.2019.104350

7. J. Wang, L. Zhang, L. Yu, Z. Jiao, H. Xie et al., A bi-functional device for self-powered electrochromic window and self-rechargeable transparent battery applications. Nat. Commun. **5**, 4921 (2014). https://doi.org/10.1038/ncomms5921

8. S. Zhang, S. Cao, T. Zhang, J.Y. Lee, Plasmonic oxygen-deficient $TiO_{2-x}$ nanocrystals for dual-band electrochromic smart windows with efficient energy recycling. Adv. Mater. **32**, e2004686 (2020). https://doi.org/10.1002/adma.202004686

9. S. Zhou, S. Wang, S. Zhou, H. Xu, J. Zhao et al., An electrochromic supercapacitor based on an MOF derived hierarchical-porous NiO film. Nanoscale **12**, 8934–8941 (2020). https://doi.org/10.1039/d0nr01152e

10. Y. Lee, J. Yun, M. Seo, S.J. Kim, J. Oh et al., Full-color-tunable nanophotonic device using electrochromic tungsten trioxide thin film. Nano Lett. **20**, 6084–6090 (2020). https://doi.org/10.1021/acs.nanolett.0c02097

11. S. Heo, C.J. Dahlman, C.M. Staller, T. Jiang, A. Dolocan et al., Enhanced coloration efficiency of electrochromic tungsten oxide nanorods by site selective occupation of sodium ions. Nano Lett. **20**, 2072–2079 (2020). https://doi.org/10.1021/acs.nanolett.0c00052

12. R.T. Wen, G.A. Niklasson, C.G. Granqvist, Eliminating electrochromic degradation in amorphous $TiO_2$ through Li-Ion detrapping. ACS Appl. Mater. Interfaces **8**, 5777–5782 (2016). https://doi.org/10.1021/acsami.6b00457

13. H.Y. Wang, H.Y. Chen, Y.Y. Hsu, U. Stimming, H.M. Chen et al., Modulation of crystal surface and lattice by doping: achieving ultrafast metal-ion insertion in anatase $TiO_2$. ACS Appl. Mater. Interfaces **8**, 29186–29193 (2016). https://doi.org/10.1021/acsami.6b11185

14. Z. Tong, Y. Tian, H. Zhang, X. Li, J. Ji et al., Recent advances in multifunctional electrochromic energy storage devices and photoelectrochromic devices. Sci. China Chem. **60**, 13–37 (2016). https://doi.org/10.1007/s11426-016-0283-0

15. W. Zhang, H. Li, W.W. Yu, A.Y. Elezzabi, Transparent inorganic multicolour displays enabled by zinc-based electrochromic devices. Light Sci. Appl. **9**, 121 (2020). https://doi.org/10.1038/s41377-020-00366-9

16. Q. Huang, S. Cao, Y. Liu, Y. Liang, J. Guo et al., Boosting the $Zn^{2+}$-Based electrochromic properties of tungsten oxide through morphology control. Sol. Energy Mater. Sol. Cells **220**, 110853 (2021). https://doi.org/10.1016/j.solmat.2020.110853

17. F. Wan, L. Zhang, X. Dai, X. Wang, Z. Niu et al., Aqueous rechargeable zinc/sodium vanadate batteries with enhanced performance from simultaneous insertion of dual carriers. Nat. Commun. **9**, 1656 (2018). https://doi.org/10.1038/s41467-018-04060-8

18. T. Koketsu, J. Ma, B.J. Morgan, M. Body, C. Legein et al., Reversible magnesium and aluminium ions insertion in cation-deficient anatase $TiO_2$. Nat. Mater. **16**, 1142–1148 (2017). https://doi.org/10.1038/nmat4976

19. M. Kazazi, P. Abdollahi, M. Mirzaei-Moghadam, High surface area $TiO_2$ nanospheres as a high-rate anode material for aqueous aluminium-ion batteries. Solid State Ionics **300**, 32–37 (2017). https://doi.org/10.1016/j.ssi.2016.11.028

20. H. Li, C.J. Firby, A.Y. Elezzabi, Rechargeable aqueous hybrid $Zn^{2+}/Al^{3+}$ electrochromic batteries. Joule **3**, 2268–2278 (2019). https://doi.org/10.1016/j.joule.2019.06.021

21. N. Zhu, F. Wu, Z. Wang, L. Ling, H. Yang et al., Reversible $Al^{3+}$ storage mechanism in anatase $TiO_2$ cathode material for ionic liquid electrolyte-based aluminum-ion batteries. J. Energy Chem. **51**, 72–80 (2020). https://doi.org/10.1016/j.jechem.2020.03.032

22. T.S. Le, T.H. Hoa, D.Q. Truong, Shape-controlled f-doped $TiO_2$ nanocrystals for Mg-ion batteries. J. Electroanal. Chem. **848**, 113293 (2019). https://doi.org/10.1016/j.jelechem.2019.113293

23. P. Hu, M. Yan, T. Zhu, X. Wang, X. Wei et al., $Zn/V_2O_5$ aqueous hybrid-ion battery with high voltage platform and long cycle life. ACS Appl. Mater. Interfaces **9**, 42717–42722 (2017). https://doi.org/10.1021/acsami.7b13110

24. Y. Tian, W. Zhang, S. Cong, Y. Zheng, F. Geng et al., Unconventional aluminum ion intercalation/deintercalation for fast switching and highly stable electrochromism. Adv. Funct. Mater. **25**, 5833–5839 (2015). https://doi.org/10.1002/adfm.201502638

25. X. Ju, F. Yang, X. Zhu, X. Jia, Zinc ion intercalation/deintercalation of metal organic framework-derived nanostructured NiO@C for low-transmittance and high-performance electrochromism. ACS Sustainable Chem. Eng. **8**, 12222–12229 (2020). https://doi.org/10.1021/acssuschemeng.0c03837

26. H. Li, W. Zhang, A.Y. Elezzabi, Transparent zinc-mesh electrodes for solar-charging electrochromic windows. Adv. Mater. **32**, e2003574 (2020). https://doi.org/10.1002/adma.202003574

27. H. Li, L. McRae, C.J. Firby, A.Y. Elezzabi, Rechargeable aqueous electrochromic batteries utilizing ti-substituted tungsten molybdenum oxide based $Zn^{2+}$ ion intercalation cathodes. Adv. Mater. **31**, e1807065 (2019). https://doi.org/10.1002/adma.201807065

28. C. Xia, J. Guo, Y. Lei, H. Liang, C. Zhao et al., Rechargeable aqueous zinc-ion battery based on porous framework zinc pyrovanadate intercalation cathode. Adv. Mater. **30**, 1705580 (2018). https://doi.org/10.1002/adma.201705580

29. L.E. Blanc, D. Kundu, L.F. Nazar, Scientific challenges for the implementation of Zn-ion batteries. Joule **4**, 771–799 (2020). https://doi.org/10.1016/j.joule.2020.03.002

30. T. Xiong, Y. Zhang, W.S.V. Lee, J. Xue, Defect engineering in manganese-based oxides for aqueous rechargeable Zinc-Ion batteries: a review. Adv. Energy Mater. **10**, 2001769 (2020). https://doi.org/10.1002/aenm.202001769

31. Y. Shi, Y. Chen, L. Shi, K. Wang, B. Wang et al., An overview and future perspectives of rechargeable zinc batteries. Small **16**, e2000730 (2020). https://doi.org/10.1002/smll.202000730

32. Y. Li, W. Yang, W. Yang, Z. Wang, J. Rong et al., Towards high-energy and anti-self-discharge Zn-Ion hybrid supercapacitors with new understanding of the electrochemistry. Nano-Micro Lett. **13**, 95 (2021). https://doi.org/10.1007/s40820-021-00625-3

33. S.M. Islam, C.J. Barile, Dynamic Windows using reversible zinc electrodeposition in neutral electrolytes with high opacity and excellent resting stability. Adv. Energy Mater. **11**, 2100417 (2021). https://doi.org/10.1002/aenm.202100417

34. L. Zhang, D. Chao, P. Yang, L. Weber, J. Li et al., Flexible pseudocapacitive electrochromics via inkjet printing of additive-free tungsten oxide nanocrystal ink. Adv. Energy Mater. **10**, 2000142 (2020). https://doi.org/10.1002/aenm.202000142

35. P. He, G. Zhang, X. Liao, M. Yan, X. Xu et al., Sodium Ion stabilized vanadium oxide nanowire cathode for high-performance Zinc-ion batteries. Adv. Energy Mater. **8**, 1702463 (2018). https://doi.org/10.1002/aenm.201702463

36. S. Liu, X. Qu, Construction of nanocomposite film of dawson-type polyoxometalate and $TiO_2$ Nanowires for electrochromic applications. Appl. Surf. Sci. **412**, 189–195 (2017). https://doi.org/10.1016/j.apsusc.2017.03.244

37. S. Cao, S. Zhang, T. Zhang, J.Y. Lee, Fluoride-assisted synthesis of plasmonic colloidal Ta-doped $TiO_2$ nanocrystals for near-infrared and visible-light selective electrochromic modulation. Chem. Mater. **30**, 4838–4846 (2018). https://doi.org/10.1021/acs.chemmater.8b02196

38. T. Dhandayuthapani, R. Sivakumar, R. Ilangovan, C. Gopalakrishnan, C. Sanjeeviraja et al., High coloration efficiency, high reversibility and fast switching response of nebulized spray deposited anatase $TiO_2$ thin films for electrochromic applications. Electrochim. Acta **255**, 358–368 (2017). https://doi.org/10.1016/j.electacta.2017.09.187

39. K.R. Reyes-Gil, Z.D. Stephens, V. Stavila, D.B. Robinson, Composite $WO_3/TiO_2$ nanostructures for high electrochromic activity. ACS Appl. Mater. Interfaces **7**, 2202–2213 (2015). https://doi.org/10.1021/am5050696

40. W. Li, G. Wu, C.M. Araújo, R.H. Scheicher, A. Blomqvist et al., $Li^+$ Ion conductivity and diffusion mechanism in $\alpha$-$Li_3N$ and $\beta$-$Li_3N$. Energy Environ. Sci. **3**, 1524 (2010). https://doi.org/10.1039/c0ee00052c

41. F. Wang, Y. Han, C.S. Lim, Y. Lu, J. Wang et al., Simultaneous phase and size control of upconversion nanocrystals through lanthanide doping. Nature **463**, 1061–1065 (2010). https://doi.org/10.1038/nature08777

42. S. Cao, S. Zhang, T. Zhang, A. Fisher, J.Y. Lee, Metal-doped $TiO_2$ colloidal nanocrystals with broadly tunable plasmon resonance absorption. J. Mater. Chem. C **6**, 4007–4014 (2018). https://doi.org/10.1039/c8tc00185e

43. L. De Trizio, R. Buonsanti, A.M. Schimpf, A. Llordes, D.R. Gamelin et al., Nb-doped colloidal $TiO_2$ nanocrystals with tunable infrared absorption. Chem. Mater. **25**, 3383–3390 (2013). https://doi.org/10.1021/cm402396c

44. L.J. Hardwick, M. Holzapfel, P. Novák, L. Dupont, E. Baudrin, Electrochemical lithium insertion into anatase-type $TiO_2$: an in situ raman microscopy investigation. Electrochim. Acta **52**, 5357–5367 (2007). https://doi.org/10.1016/j.electacta.2007.02.050

45. R.T. Wen, C.G. Granqvist, G.A. Niklasson, Eliminating degradation and uncovering Ion-trapping dynamics in electrochromic $WO_3$ thin films. Nat. Mater. **14**, 996–1001 (2015). https://doi.org/10.1038/nmat4368

46. M. Ni, D. Sun, X. Zhu, Q. Xia, Y. Zhao et al., Fluorine triggered surface and lattice regulation in anatase $TiO_{2-x}F_x$ nanocrystals for ultrafast pseudocapacitive sodium storage. Small **16**, e2006366 (2020). https://doi.org/10.1002/smll.202006366

47. C.J. Dahlman, Y. Tan, M.A. Marcus, D.J. Milliron, Spectroelectrochemical signatures of capacitive charging and ion insertion in doped anatase titania nanocrystals. J. Am. Chem. Soc. **137**, 9160–9166 (2015). https://doi.org/10.1021/jacs.5b04933

48. L.F. Wan, D. Prendergast, Ion-pair dissociation on $\alpha$-$MoO_3$ Surfaces: focus on the electrolyte–cathode compatibility issue in Mg batteries. J. Phys. Chem. C **122**, 398–405 (2017). https://doi.org/10.1021/acs.jpcc.7b09124

49. C. Legein, B.J. Morgan, F. Fayon, T. Koketsu, J. Ma et al., Atomic insights into Aluminium-Ion insertion in defective anatase for batteries. Angew. Chem. Int. Ed. **59**, 19247–19253 (2020). https://doi.org/10.1002/anie.202007983

50. S. Zhang, S. Cao, T. Zhang, A. Fisher, J.Y. Lee, $Al^{3+}$ intercalation/de-intercalation-enabled dual-band electrochromic smart windows with a high optical modulation, quick response and long cycle Life. Energy Environ. Sci. **11**, 2884–2892 (2018). https://doi.org/10.1039/c8ee01718b